



| | |
|------------------|---|
| Title | Bragg-edge neutron transmission spectrum analysis using a high-speed-camera-type time-of-flight neutron imaging detector |
| Author(s) | Sato, Hirotaka; Mochiki, Koh-ichi; Tanaka, Kenta; Ishizuka, Ken; Ishikawa, Hirotaku; Kamiyama, Takashi; Kiyanagi, Yoshiaki |
| Citation | Nuclear Instruments and Methods in Physics Research Section A : Accelerators, Spectrometers, Detectors and Associated Equipment, 943, 162501 https://doi.org/10.1016/j.nima.2019.162501 |
| Issue Date | 2019-11-01 |
| Doc URL | http://hdl.handle.net/2115/83121 |
| Rights | © 2019, Elsevier. Licensed under the Creative Commons Attribution-NonCommercial-NoDerivatives 4.0 International http://creativecommons.org/licenses/by-nc-nd/4.0/ |
| Rights(URL) | http://creativecommons.org/licenses/by-nc-nd/4.0/ |
| Type | article (author version) |
| File Information | NIM-A_knife-phase_sato_v7.pdf |



[Instructions for use](#)

1 **Bragg-edge neutron transmission spectrum analysis** 2 **using a high-speed-camera-type time-of-flight neutron** 3 **imaging detector**

4
5 Hiroataka Sato^{1,*}, Koh-ichi Mochiki², Kenta Tanaka², Ken Ishizuka², Hirotaiku Ishikawa¹,
6 Takashi Kamiyama¹ and Yoshiaki Kiyonagi³

7
8 ¹Graduate School of Engineering, Hokkaido University, Kita-13 Nishi-8, Kita-ku,
9 Sapporo 060-8628, Japan

10 ²Graduate School of Engineering, Tokyo City University, 1-28-1 Tamatutumi, Setagaya-
11 ku, Tokyo 158-8557, Japan

12 ³Graduate School of Engineering, Nagoya University, Furo-cho, Chikusa-ku, Nagoya
13 464-8603, Japan

14
15 *Corresponding author. Tel.: +81-11-706-6679; Fax: +81-11-706-6679.

16 E-mail address: h.sato@eng.hokudai.ac.jp

17 18 **Abstract**

19 Thus far, quantitative imaging of crystallographic information using a time-of-flight
20 (TOF) neutron Bragg-edge transmission method has been performed using counting-type
21 neutron TOF-imaging detectors. However, at intense pulsed neutron beam facilities, the
22 limit of the maximum counting rate of the detectors restricts acceptable neutron intensity.
23 A camera-type neutron imaging detector can accept considerably higher neutron intensity
24 than counting-type detectors. For this reason, a camera-type detector applicable for the
25 TOF measurement has been developed. However, the camera-type detector has not been
26 applied to quantitative analysis of crystallographic information thus far. As the neutron
27 spectrum data obtained by a camera-type detector may have different characteristics
28 compared with those obtained by a counting-type detector, it is important to
29 experimentally demonstrate the applicability of the camera-type detector for quantitative
30 crystallographic analysis. Thus, in this study, we performed a demonstration experiment
31 using a steel knife specimen at a beam-line connected to a coupled-type neutron
32 moderator of the Hokkaido University Neutron Source (HUNS). We applied the Rietveld-
33 type data analysis method to measured Bragg-edge neutron transmission spectra in order
34 to obtain quantitative crystallographic information, and we then conducted the crystalline
35 phase imaging. Finally, using the new detector system along with the spectral analysis,
36 the results were obtained non-destructively; the results showed that the crystalline phase

37 distribution of the steel knife composed of two phases was changed gradually, and the
38 crystallographic texture and crystallite size distributions were almost uniform. In addition,
39 the new detector system provided the best spatial resolution of 520 μm at a field-of-view
40 of 13 cm \times 13 cm.

41

42 **Keywords:** Time-of-flight neutron imaging detector; High speed camera; Pulsed neutron
43 Bragg-edge transmission imaging; Quantitative crystallographic information analysis

44

45 **1. Introduction**

46 Pulsed neutron Bragg-edge transmission imaging using the time-of-flight (TOF)
47 method is a unique material characterization tool that can simultaneously visualize
48 quantitative crystallographic information in a bulk material over a large area with spatial
49 resolution [1-6]. Therefore, construction projects of energy-resolved neutron imaging
50 instruments at accelerator-driven intense pulsed spallation sources are in progress, e.g., J-
51 PARC MLF BL22 “RADEN” [7], RAL ISIS-TS2 “IMAT” [8] and ESS “ODIN” [9].
52 However, at intense beam facilities, the limit of the maximum counting rate of counting-
53 type neutron TOF-imaging detectors, such as the scintillator pixel type [10], gas electron
54 multiplier (GEM) type [11], micro-pixel chamber (μPIC) type [12] and micro-channel
55 plate (MCP) type [13], is not sufficient for measuring neutron transmission TOF spectra
56 toward the full open beam.

57 For this reason, camera-type detectors, which are currently used at nuclear reactor-
58 based intense neutron sources, are expected. Of course, for measuring neutron
59 transmission TOF spectra, the camera should have a characteristic of a high frame rate
60 (high-speed camera [14]) of the 10,000-fps class. However, as the volume of image data
61 becomes immense, conducting long duration experiments is challenging. Thus, in a
62 previous study [15], we developed a new neutron TOF-imaging detector equipped with a
63 new high-speed camera system combined with the neutron color image intensifier [16].
64 This camera has a seamless accumulation system that can reduce the volume of data by
65 the image accumulator, and continuously store the data in the memory during the
66 experiment. Using this system, the long-time measurement of approximately 100 hours
67 is feasible. In addition, this detector is expected to achieve the finest pixel size of 520 μm
68 and a field-of-view (FOV) of 13 cm \times 13 cm in Bragg-edge neutron transmission imaging
69 experiments, which are better than those achieved by the GEM detector (pixel size of 800
70 μm and FOV of 10 cm \times 10 cm). Furthermore, recently, higher spatial resolution
71 techniques for this camera-type detector, namely, center-of-gravity calculation and super-
72 resolution processing, have been developed [17].

73 However, one of the important final goals of neutron TOF-imaging experiments is

74 actual quantitative evaluation of material information through neutron transmission
75 spectrum analysis. For this purpose, in this study, we conducted an experiment to measure
76 a steel knife specimen by using this camera system at a beam-line connected to a pulsed
77 neutron source based on a coupled-type neutron moderator [18] and driven by a compact
78 electron accelerator, the Hokkaido University Neutron Source (HUNS) [19]. Then,
79 crystalline phase analyses with texture/extinction corrections using the Bragg-edge
80 neutron transmission spectrum analysis program, RITS [2,20,21], were performed to
81 demonstrate the applicability of the new camera-type detector. As a result, we could
82 successfully obtain detailed information of the knife specimen by using this detector
83 through spectrum analysis. In this paper, we report the details of the experiment and the
84 data analysis.

85

86 **2. High-speed camera detector for time-of-flight neutron imaging**

87 To conduct efficient neutron TOF-imaging experiments using camera-type detectors,
88 two important requirements must be considered. One is neutron and optical image
89 intensifiers to obtain sufficient brightness at every neutron pulse. The other is a seamless
90 accumulation system for many neutron images of the same TOF channel obtained during
91 the long duration of irradiation. In this section, details of the implementation of both the
92 image intensifiers and the seamless accumulation system in the new high-speed camera
93 system are presented.

94 Fig. 1 presents a schematic layout of the high-frame-rate CMOS camera system
95 combined with the neutron color image intensifier. The neutron color image intensifier
96 [16] used in this system was TCN9100B made by TOSHIBA. The maximum FOV was
97 22.86 cm diameter, and the best achievable spatial resolution was $< 30 \mu\text{m}$. The input
98 window for neutron-electron conversion was prepared with B_4C , comprising 99.7%
99 enriched ^{10}B . The electrons were focused on the output window using an electron lens,
100 and then the visible light was emitted from the output window. The FOV of the input
101 window detected by the output window using the electron lens can be selected from three
102 diameters, namely, 22.86, 17.78, 13.97 cm. The output window consisted of a short
103 afterglow phosphor, $\text{Y}_2\text{SiO}_5:\text{Ce}$ (with a decay time of $5 \mu\text{s}$). This neutron image intensifier
104 had a high-speed gating function to avoid burst neutron/gamma-ray flashes emitted from
105 a neutron source.

106 Through the optical mirror and lens, the optical image was intensified by the optical
107 image intensifier C9547-02 MOD using an MCP with a short afterglow phosphor P46
108 (HAMAMATSU). This optical image intensifier also had a high-speed gating function to
109 avoid extremely bright images caused by burst neutron/gamma-ray flashes emitted from
110 a neutron source. Through the optical mirror and lens, the optical image was captured by

111 a high-frame-rate CMOS camera, MEMRECAM ST-821-HX (NAC Image Technology).

112 In this camera-type neutron TOF-imaging system, the pixel size and time resolution
113 can be selected in principle as follows:

114 1. The number of pixels is 320×240 ($572 \mu\text{m}$ pixel size in a 22.86 cm diameter FOV
115 and $349 \mu\text{m}$ pixel size in a 13.97 cm diameter FOV) in case the time resolution is 10
116 μs (100 kfps mode).

117 2. The number of pixels is 512×512 ($316 \mu\text{m}$ pixel size in a 22.86 cm diameter FOV
118 and $193 \mu\text{m}$ pixel size in a 13.97 cm diameter FOV) in case the time resolution is
119 $33.3 \mu\text{s}$ (30 kfps mode).

120 3. The number of pixels is 960×960 ($169 \mu\text{m}$ pixel size in a 22.86 cm diameter FOV
121 and $103 \mu\text{m}$ pixel size in a 13.97 cm diameter FOV) in case the time resolution is 100
122 μs (10 kfps mode).

123 The demonstration experiment presented in this paper was conducted in the second mode
124 (30 kfps mode). The timings of both the accelerator (pulsed neutron source) and the
125 camera (pulsed neutron TOF-imaging detector) were controlled under the same trigger
126 control system.

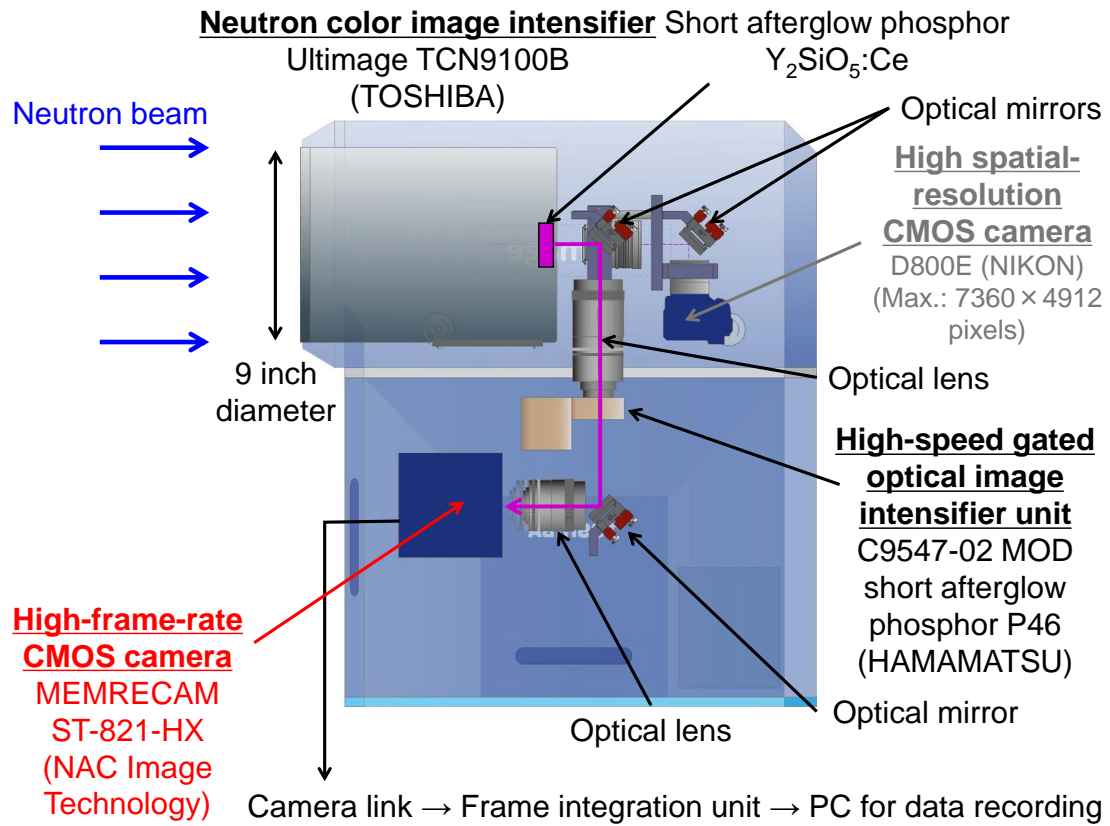
127 Finally, details of the seamless accumulation system for the high-speed camera are
128 presented. This system has a specialized image accumulation system (the frame
129 integration unit in Fig. 1). Concretely, a certain TOF-channel image that is accumulated
130 by 4096 neutron pulses has a 24-bit data length. Therefore, for example, in case the 100
131 kfps mode (the highest capturing speed) is used at an accelerator facility of 50 pulses per
132 second such as HUNS, the data length becomes $24 \text{ bit} \times 2,000$ ($100,000 / 50 = 2,000$
133 frames per pulse) in 82 seconds ($4,096 / 50 = 82$). The data length of $24 \text{ bit} \times 2,000$
134 corresponds to a data file of 3,570 Mbit. A data volume of 44 Mbit/s ($= 3,570 \text{ Mbit} / 82$
135 seconds), which corresponds to 5.6 MByte/s in this system, is continuously generated.
136 However, as this system has a 2 TByte memory, the capturing of images continuously
137 (seamlessly) for approximately 100 hours is feasible; 100 hours is usually sufficient for
138 Bragg-edge transmission imaging experiments.

139 The neutron transmission TOF spectrum of a certain pixel, $Tr(tof)$, is obtained by the
140 following calculation:

141
$$Tr(tof) = \frac{I_{\text{sample}}(tof) - I_{\text{dark}}(tof)}{I_{\text{direct}}(tof) - I_{\text{dark}}(tof)} .$$

142 Here, $I_{\text{sample}}(tof)$ is the TOF-dependent signal measured with the sample in a neutron beam,
143 $I_{\text{direct}}(tof)$ is the TOF-dependent signal measured without the sample in a neutron beam,
144 and $I_{\text{dark}}(tof)$ is the TOF-dependent signal measured without neutron production.

145



146

147 Fig. 1. Configuration of the neutron color image intensifier and the high-frame-rate
148 CMOS camera with the seamless accumulation function for a time-of-flight neutron
149 transmission imaging experiment.

150

151 3. Neutron TOF-imaging experiment

152

153 3.1. Experimental setup and conditions at the Hokkaido University Neutron Source

154 In this study, we used a relatively weak pulsed neutron source, the Hokkaido University
155 Neutron Source (HUNS). We adopted the HUNS facility in this study for the following
156 reasons: The main reason is to avoid the radio-activation of the new detector system
157 before completion of the feasibility study. The second reason is that HUNS is one of the
158 pioneering and reliable facilities and its facility has been used many times for the Bragg-
159 edge neutron transmission imaging. The third reason is that the experiment would be
160 successfully performed at intense pulsed neutron sources if the experiment could be done
161 at the relatively weak pulsed neutron source.

162 The experimental setup was very simple, and quite similar to a layout described in Ref.
163 [22]. Here, the key parameters are presented.

164 Fig. 2 shows a schematic layout of the neutron TOF-imaging experiment performed in
165 this study. The experiment was performed at HUNS installed at the 1-kW class electron

166 linear accelerator facility (Hokkaido LINAC) at Hokkaido University in Japan [19]. The
167 pulse width of the electron beam was 3 μs , and the pulse repetition rate used was 50 Hz.
168 Neutrons were generated through photonuclear reactions. The number of generated fast
169 neutrons emitted from the neutron production target was approximately 10^{12} n/s. The
170 generated fast neutrons were moderated to cold neutrons in a 20 K mesitylene-based
171 main-moderator (5 cm thickness, 10 cm \times 10 cm area) surrounded by polyethylene pre-
172 moderators of 1.5 cm thickness. The graphite (inside) and lead (outside) reflectors
173 surrounded the outside of moderators. A wing geometry was used in an arrangement
174 between a target and a moderator in order to suitably secure the line-of-sight. Here, we
175 used a coupled-type moderator to obtain higher cold neutron intensity [18]. As a result, a
176 broad neutron pulse was emitted from the neutron source; about 170 μs in the pulse
177 FWHM for cold neutrons. The moderated neutrons were transported to the
178 sample/detector position through an evacuated tube of 3 m length. The total flight path
179 length of neutrons was 5.8 m. The neutron flux at the detector position was approximately
180 10^4 n/cm²/s. The wavelength resolution at the wavelength region of cold neutrons was
181 3%, which was not high wavelength resolution compared with that obtained for an
182 instrument at a long flight path length viewing a decoupled-type moderator. The
183 collimator ratio, L/D, was approximately 58 (17 mrad in the beam angular divergence)
184 because there were no pinhole collimators in the beam-line. The beam size became larger
185 than 10 cm \times 10 cm (the moderator surface area) due to the divergence.

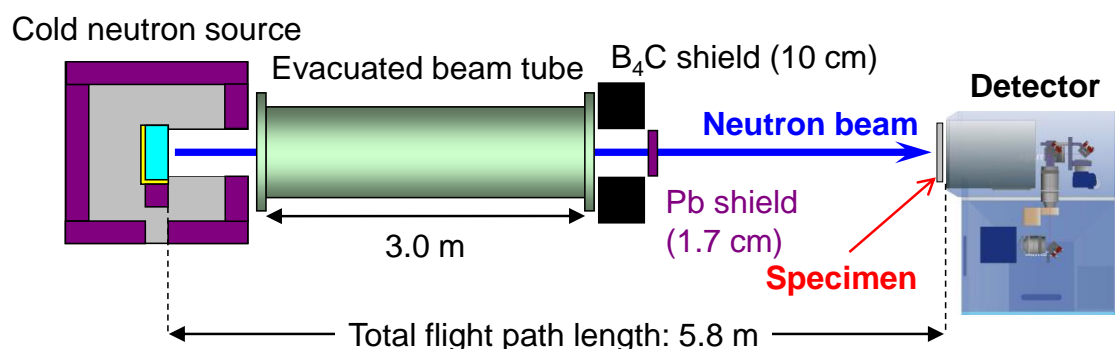
186 The neutron image intensifier (NII) combined with a high-speed camera system was
187 operated in the 22.86 cm diameter FOV NII-mode with the 30 kfps camera-mode (number
188 of pixels was 512 \times 512, and the time resolution was 33.3 μs). In fact, for the reduction
189 of statistical errors, crystalline phase analysis/imaging using the Rietveld-type spectral
190 fitting analysis was performed in 256 \times 256 pixels and the 66.6 μs TOF channel width. In
191 conclusion, after the measurement, we found that the actual achieved pixel size was 520
192 μm and FOV was 13.3 cm \times 13.3 cm. In any case, the pixel size is the finest in such large
193 FOV condition for the measurement of Bragg-edge transmission imaging at pulsed
194 neutron sources.

195 To reduce burst gamma-ray flashes, we set a lead plate of 1.7 cm thickness in the beam-
196 line. In addition, to avoid burst neutron/gamma-ray flashes, the NII was operated from 1
197 ms to 11 ms after the burst (neutron wavelength region 0.07-0.75 nm). The optical image
198 intensifier was operated from 2 ms to 7 ms after the burst (neutron wavelength region
199 0.14-0.48 nm, which is an actual usable neutron wavelength range).

200 The measurement time of an open beam for data normalization was 12 hours, and the
201 measurement time of an in-sample beam was 15 hours. These values were normal for the
202 pulsed neutron Bragg-edge transmission imaging at HUNS. The specimen was directly

203 coupled to the imaging detector.

204



205

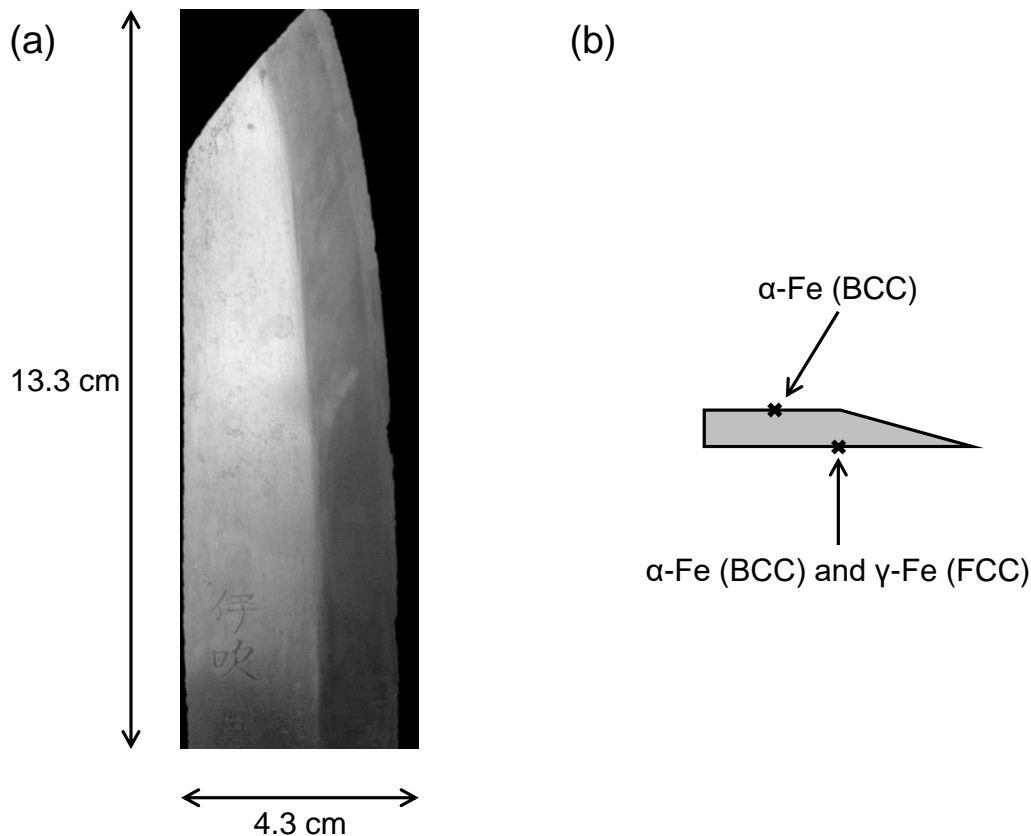
206 Fig. 2. Schematic layout of the neutron TOF-imaging experiment.

207

208 3.2. Specimen

209 Fig. 3 (a) shows a photograph of the specimen, which was a kitchen knife “Seki-no-
210 magoroku” made in Japan. Here, we aimed to study the feasibility of the new detector
211 system through a spectral analysis of Bragg-edge neutron transmission imaging. The
212 analysis can provide the crystallographic texture and crystallite size of each crystalline
213 phase at the wavelength resolution used in this study, and crystal lattice strain at a higher
214 wavelength resolution of several times of 0.1%. Thus, we analyzed the full information
215 at the wavelength resolution used in this study, namely, the crystallographic textures and
216 crystallite sizes of two crystalline phases. We chose a new suitable specimen for this
217 purpose. This knife specimen was suitable because it consisted of two crystalline phases
218 according to X-ray diffraction measurements performed using D8 DISCOVER with
219 GADDS (BRUKER AXS) with a cobalt $K\alpha_1$ target (0.1789 nm wavelength) and a 0.8
220 mm tungsten collimator. Two irradiation points (with a spot size approximately 1 mm^2)
221 were studied at one side and the reverse side of the knife. The results indicate that this
222 knife consists of two crystalline phases of iron; α -Fe phase (BCC: body-centered cubic
223 crystal structure) and γ -Fe phase (FCC: face-centered cubic crystal structure). In addition,
224 different quantities of each phase between one side and the reverse side of the specimen
225 were observed; one side consists of only α -Fe, and the other side consists of both α -Fe
226 and γ -Fe (see Fig. 3 (b)). Thus, the X-ray diffraction studies revealed that we can
227 demonstrate the feasibility of the new camera-type TOF-imaging detector toward
228 quantitative imaging of crystalline phases (as well as their crystallographic textures and
229 crystallite sizes) by using this complex steel sample.

230



231

232 Fig. 3. (a) Photograph of the kitchen knife “Seki-no-magoroku” sample. (b) Cross-
 233 sectional picture of the sample. This sample contains two crystalline phases, α -Fe (BCC)
 234 and γ -Fe (FCC).

235

236 4. Results and discussion

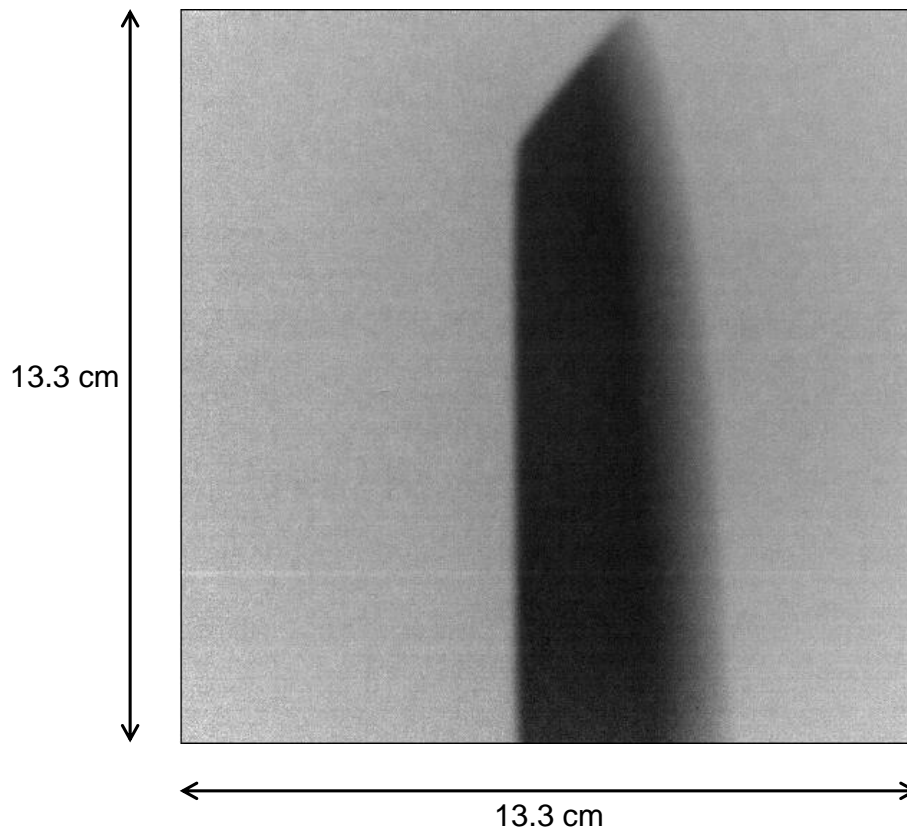
237 In the experiment conducted in this study, the ratio of $I_{\text{direct}}(\text{tof})$ to $I_{\text{dark}}(\text{tof})$ was 1.004
 238 at the neutron wavelength of 0.2 nm due to low neutron flux. The neutron transmission
 239 evaluated by pixels at the direct beam region successfully corresponded to 1.0. The
 240 statistical error was approximately 2% for a single TOF channel (66.6 μs) of a single pixel
 241 (520 μm). Further detailed evaluations about measured neutron transmission spectra are
 242 discussed in Sec. 4.2. In the following sections, we describe the experimental and analysis
 243 results in more detail.

244

245 4.1. Neutron transmission image

246 Fig. 4 shows a conventional white neutron radiograph. This image was visualized in a
 247 pixel size of 260 μm (number of pixels was 512×512). The FOV was 13.3 cm \times 13.3 cm.
 248 We observe that the sample thickness decreases near the cutting edge.

249



250

251 Fig. 4. White neutron radiograph of the kitchen knife sample, obtained by the present
 252 imaging detector. The pixel size is $260\ \mu\text{m}$, and the number of pixels is 512×512 .

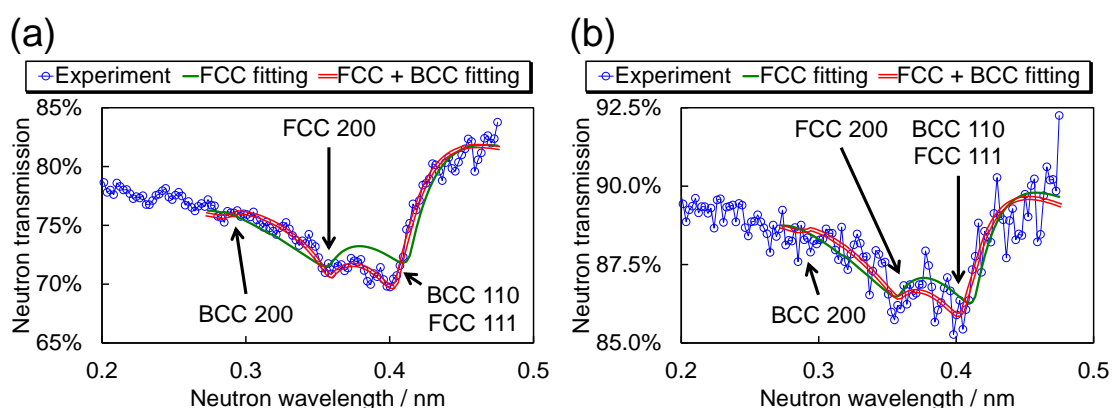
253

254 **4.2. Bragg-edge neutron transmission spectrum and its Rietveld-type analysis**

255 We observed and analyzed the Bragg-edge neutron transmission spectra of the blade
 256 body and the cutting edge of the knife sample. Fig. 5 shows the Bragg-edge neutron
 257 transmission spectra of (a) the thick blade body and (b) the thin cutting edge, measured
 258 by some pixels' summation of the high-speed camera detector. Note that Bragg-edges are
 259 broadened due to the low wavelength resolution caused by the coupled moderator (see
 260 Ref. [22]).

261 First, we clearly observe two Bragg-edges at wavelengths $0.36\ \text{nm}$ and $0.41\ \text{nm}$. The
 262 candidates of the $0.41\ \text{nm}$ Bragg-edge are $\alpha\text{-Fe}$ (BCC) $\{110\}$ ($0.405\ \text{nm}$) and $\gamma\text{-Fe}$ (FCC)
 263 $\{111\}$ ($0.41\ \text{nm}$). By contrast, the candidate of the $0.36\ \text{nm}$ Bragg-edge is only $\gamma\text{-Fe}$ $\{200\}$
 264 ($0.36\ \text{nm}$). Therefore, we conducted the profile fitting analysis based on $\gamma\text{-Fe}$. The
 265 Rietveld-type fitting analysis program that we used here was Rietveld Imaging of
 266 Transmission Spectra (RITS) [2,20,21]. The instrumental resolution function in the RITS
 267 program, which expresses Bragg-edge broadening due to the low wavelength resolution,
 268 had the same parameters previously obtained by an experiment conducted using a
 269 counting-type neutron detector (GEM-type detector [11]) at the same beam-line. As

270 expected, profile fitting based on the single phase (γ -Fe) could not reconstruct the
 271 experimental transmission intensities over the wide wavelength bandwidth (see solid
 272 single-lines (FCC fitting) in Fig. 5). Next, we assumed the double phases, γ -Fe and α -Fe,
 273 as expected by X-ray diffraction studies. The solid double-lines (FCC + BCC fitting) in
 274 Fig. 5 show the profile fitting curves. In particular, Fig. 5 (a) clearly indicates that this
 275 assumption could well reconstruct the experimental transmission intensities over the wide
 276 wavelength bandwidth. This implies that Bragg-edge neutron transmission spectra
 277 measured by this camera system can successfully identify the existence of each crystalline
 278 phase in a material composed of multiple phases.
 279



280
 281 Fig. 5. Bragg-edge neutron transmission spectra measured by some pixels' summation of
 282 the present imaging detector. The fitting curves were given by the RITS program. (a)
 283 Thick blade body. (b) Thin cutting edge. The FCC and BCC double-phase assumption
 284 can give a better fitting curve. Incidentally, fluctuations of the experimental data of Fig.
 285 5 (b) were caused by statistical errors. The fluctuations are emphasized due to
 286 enlargement of the vertical axis of Fig. 5 (b) (the plotted range is 7.5%) compared with
 287 that of Fig. 5 (a) (the plotted range is 20%). The relative errors for both the data are almost
 288 the same, 0.6%-0.7%.

289

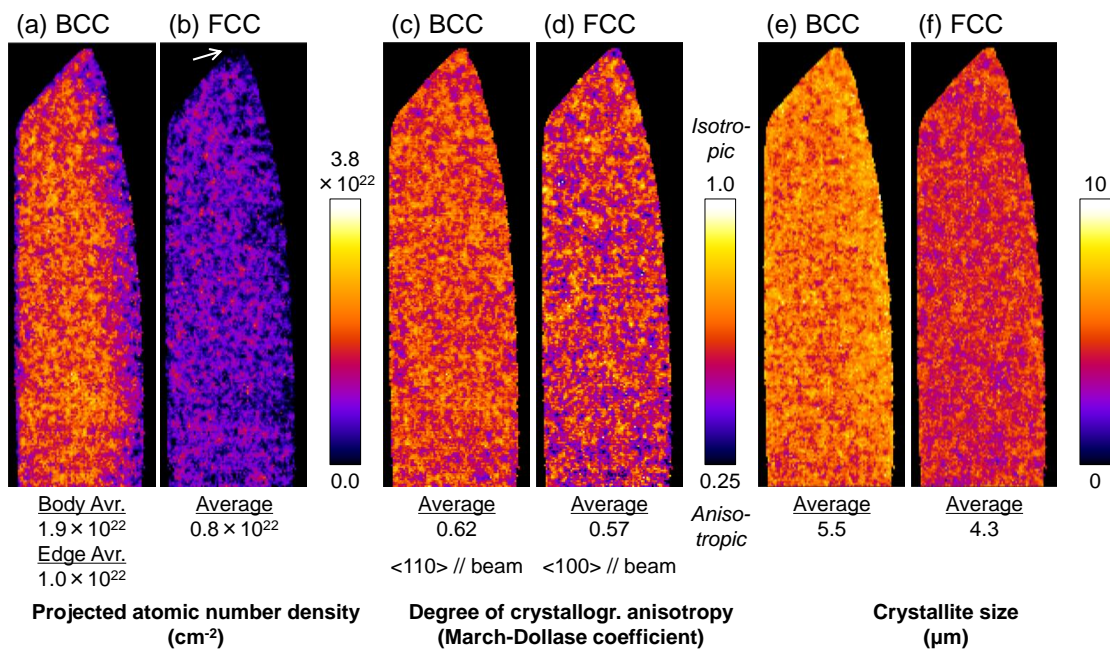
290 4.3. Crystalline phase imaging with texture and extinction corrections

291 By the transmission-spectrum profile fitting analyses over all pixels using the RITS
 292 program, quantitative images of each phase were obtained under the correction of both
 293 the texture effect and extinction effect [20]. This is because RITS has the March-Dollase
 294 preferred orientation function for the texture analysis and Sabine's primary extinction
 295 function for the crystallite size analysis [2].

296 Figs. 6 (a) and (b) show the crystalline phase imaging results of α -Fe (BCC) and γ -Fe
 297 (FCC), respectively. The imaging results were expressed by the projected atomic number
 298 density (atomic number density \times thickness) for each phase. Furthermore, by using this

299 value, the volume fraction of each phase can be derived [23].

300 Fig. 6 (a) indicates that the projected atomic number density of α -Fe reduces gradually
 301 from the blade body to the cutting edge. This trend is similar to the result of the white
 302 neutron radiograph (see Fig. 4). By contrast, the projected atomic number density of γ -Fe
 303 does not change over the whole region. At the blade body region, the projected atomic
 304 number density of γ -Fe is almost a half ($0.8 \times 10^{22} \text{ cm}^{-2}$) of that of α -Fe ($1.9 \times 10^{22} \text{ cm}^{-2}$).
 305 Meanwhile, at the cutting edge region, the projected atomic number densities of both
 306 phases are almost the same ($\sim 0.9 \times 10^{22} \text{ cm}^{-2}$). It is also interesting that γ -Fe is not present
 307 at all at the tip of the cutting edge (see the top-center region (a region indicated by a white
 308 arrow) of Fig. 6 (b)).
 309



310 Fig. 6. Quantitative imaging results of (a) α -Fe (BCC) phase and (b) γ -Fe (FCC) phase.
 311 The projected atomic number density effectively indicates the thickness variations of each
 312 phase; quantitative texture imaging results of (c) α -Fe (BCC) phase and (d) γ -Fe (FCC)
 313 phase; crystallite size imaging results of (e) α -Fe (BCC) phase and (f) γ -Fe (FCC)
 314 phase; these were obtained with the latest RITS program [21]. In these images, the pixel size is
 315 $520 \mu\text{m}$ and the field-of-view is $13.3 \text{ cm} \times 4.3 \text{ cm}$.
 316

317

318 4.4. Discussion of the whole knife structure based on phase, texture and crystallite- 319 size imaging results

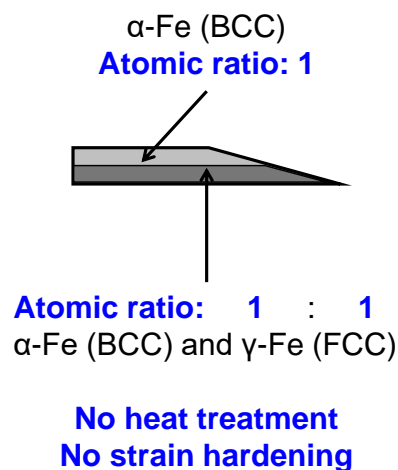
320 Figs. 6 (c) and (d) present the quantitative imaging results of crystallographic
 321 anisotropy of (c) α -Fe (BCC) phase and (d) γ -Fe (FCC) phase, expressed by the March-
 322 Dollase coefficient [2,24,25]. In addition, the RITS analyses suggested that the preferred

323 orientations parallel to the neutron beam direction were $\langle 110 \rangle$ for α -Fe and $\langle 100 \rangle$ for γ -
324 Fe. Figs. 6 (e) and (f) show crystallite size imaging results of (e) α -Fe (BCC) phase and
325 (f) γ -Fe (FCC) phase.

326 The most important point from both viewpoints of texture and crystallite size is that
327 both microstructures of each phase are almost uniform over the whole sample volume.
328 This trend is quite different from that of Japanese swords, which usually receive heat
329 treatment and strain hardening during processing and have spatial variations in terms of
330 texture and microstructure [26]. In other words, it can be deduced that the knife specimen
331 we measured did not undergo such plastic deformation.

332 According to these discussions, we finally discovered the whole structure of the knife
333 as follows. Fig. 7 shows a schematic layout of the deduced whole knife structure. First,
334 this knife did not receive any heat treatment and strain hardening, as observed from Figs.
335 6 (c)-(f). At the cutting edge, α -Fe (BCC) and γ -Fe (FCC) exist in almost the same atomic
336 quantity, as observed from Figs. 6 (a) and (b). From the edge to the body, only α -Fe (BCC)
337 gradually increases, as seen in from Figs. 6 (a) and (b). Therefore, it is estimated that two
338 types of steel plate are stacked to make this knife, as illustrated in Fig. 7. These
339 estimations are consistent with the X-ray diffraction results presented in Fig. 3 (b). This
340 confirms the reliability of the neutron experimental method using the present detector
341 system. Furthermore, the composition of each phase was obtained by the neutron Bragg-
342 edge transmission method, which could not be quantitatively obtained by the X-ray
343 diffraction. This important result indicates the usability of neutron transmission spectrum
344 analysis using the camera-type TOF-imaging neutron detector.

345



346

347 Fig. 7. A schematic layout of the whole structure of the knife specimen, as deduced from
348 the phase, texture and crystallite size imaging results.

349

350 **5. Conclusion**

351 We successfully conducted the first demonstration of quantitative crystallographic
352 information imaging using the time-of-flight (TOF) Bragg-edge transmission imaging by
353 using a camera-type detector, namely, the neutron color image intensifier combined with
354 a new high-speed camera system. The important point for the achievement is that the
355 profile analysis of the neutron spectrum over a wide wavelength bandwidth of Bragg-
356 edge transmission data (the Rietveld-type analysis) is feasible using this new detector. In
357 addition, the crystalline phase imaging was achieved under the best spatial condition at
358 the beam-line connected to the coupled-type moderator of the HUNS facility; the
359 conditions were a 520 μm pixel size and a 13.3 cm \times 13.3 cm field-of-view, which is
360 larger than the field-of-view (less than 10 cm) of counting-type detectors.

361 In the future, the developed new detector system may achieve Bragg-edge neutron
362 transmission imaging experiments of better performances at intense pulsed neutron
363 sources. For example, imaging of 260 μm pixel size, short measurement time and high
364 wavelength resolution (strain) analysis, would be further achieved with a 13.3 cm \times 13.3
365 cm field-of-view.

366

367 **Acknowledgements**

368 The authors thank Mr. Koh-ichi Sato of Hokkaido University for accelerator operations
369 and experimental assistances. This work was supported by JSPS KAKENHI Grant
370 Number 23226018.

371

372 **References**

- 373 [1] J. R. Santisteban, L. Edwards, M. E. Fitzpatrick, A. Steuwer, P. J. Withers, M. R.
374 Daymond, M. W. Johnson, N. Rhodes and E. M. Schooneveld, *Nucl. Instrum.*
375 *Methods A* **481** (2002) 765-768.
- 376 [2] H. Sato, T. Kamiyama and Y. Kiyonagi, *Mater. Trans.* **52** (2011) 1294-1302.
- 377 [3] R. Woracek, D. Penumadu, N. Kardjilov, A. Hilger, M. Boin, J. Banhart and I. Manke,
378 *Adv. Mater.* **26** (2014) 4069-4073.
- 379 [4] H. Sato, T. Sato, Y. Shiota, T. Kamiyama, A. S. Tremsin, M. Ohnuma and Y. Kiyonagi,
380 *Mater. Trans.* **56** (2015) 1147-1152.
- 381 [5] H. Sato, Y. Shiota, T. Shinohara, T. Kamiyama, M. Ohnuma, M. Furusaka and Y.
382 Kiyonagi, *Phys. Procedia* **69** (2015) 349-357.
- 383 [6] H. Sato, Y. Shiota, S. Morooka, Y. Todaka, N. Adachi, S. Sadamatsu, K. Oikawa, M.
384 Harada, S. Y. Zhang, Y. H. Su, T. Kamiyama, M. Ohnuma, M. Furusaka, T. Shinohara
385 and Y. Kiyonagi, *J. Appl. Crystallogr.* **50** (2017) 1601-1610.
- 386 [7] T. Shinohara, T. Kai, K. Oikawa, M. Segawa, M. Harada, T. Nakatani, M. Ooi, K.

- 387 Aizawa, H. Sato, T. Kamiyama, H. Yokota, T. Sera, K. Mochiki and Y. Kiyanagi, J.
388 Phys. Conf. Ser. **746** (2016) 012007.
- 389 [8] W. Kockelmann, S. Y. Zhang, J. F. Kelleher, J. B. Nightingale, G. Burca and J. A.
390 James, Phys. Procedia **43** (2013) 100-110.
- 391 [9] M. Strobl, Phys. Procedia **69** (2015) 18-26.
- 392 [10]H. Sato, O. Takada, S. Satoh, T. Kamiyama and Y. Kiyanagi, Nucl. Instrum. Methods
393 A **623** (2010) 597-599.
- 394 [11]S. Uno, T. Uchida, M. Sekimoto, T. Murakami, K. Miyama, M. Shoji, E. Nakano, T.
395 Koike, K. Morita, H. Satoh, T. Kamiyama and Y. Kiyanagi, Phys. Procedia **26** (2012)
396 142-152.
- 397 [12]J. D. Parker, M. Harada, K. Hattori, S. Iwaki, S. Kabuki, Y. Kishimoto, H. Kubo, S.
398 Kurosawa, Y. Matsuoka, K. Miuchi, T. Mizumoto, H. Nishimura, T. Oku, T. Sawano,
399 T. Shinohara, J. Suzuki, A. Takada, T. Tanimori and K. Ueno, Nucl. Instrum. Methods
400 A **726** (2013) 155-161.
- 401 [13]A. S. Tremsin, J. B. McPhate, A. Steuwer, W. Kockelmann, A. M Paradowska, J. F.
402 Kelleher, J. V. Vallerga, O. H. W. Siegmund and W. B. Feller, Strain **48** (2012) 296-
403 305.
- 404 [14]M. Segawa, M. Ooi, T. Kai, T. Shinohara, H. Satoh and M. Kureta, JPS Conf. Proc.
405 **8** (2015) 036006.
- 406 [15]K. Mochiki, K. Ishizuka, K. Morikawa, T. Kamiyama and Y. Kiyanagi, Phys.
407 Procedia **69** (2015) 143-151.
- 408 [16]K. Nittoh, C. Konagai, T. Noji and K. Miyabe, Nucl. Instrum. Methods A **605** (2009)
409 107-110.
- 410 [17]T. Uragaki, J. Koide, J. Kawarabayashi, K. Mochiki, Y. Matsumoto, Y. H. Su, K.
411 Hiroi, T. Shinohara and T. Kai, JPS Conf. Proc. **22** (2018) 011027.
- 412 [18]Y. Kiyanagi, N. Watanabe and H. Iwasa, Nucl. Instrum. Methods A **312** (1992) 561-
413 570.
- 414 [19]M. Furusaka, H. Sato, T. Kamiyama, M. Ohnuma and Y. Kiyanagi, Phys. Procedia
415 **60** (2014) 167-174.
- 416 [20]H. Sato, T. Shinohara, R. Kiyanagi, K. Aizawa, M. Ooi, M. Harada, K. Oikawa, F.
417 Maekawa, K. Iwase, T. Kamiyama and Y. Kiyanagi, Phys. Procedia **43** (2013) 186-
418 195.
- 419 [21]H. Sato, K. Watanabe, K. Kiyokawa, R. Kiyanagi, K. Y. Hara, T. Kamiyama, M.
420 Furusaka, T. Shinohara and Y. Kiyanagi, Phys. Procedia **88** (2017) 322-330.
- 421 [22]H. Sato, Y. Shiota, T. Kamiyama, M. Ohnuma, M. Furusaka and Y. Kiyanagi, Phys.
422 Procedia **60** (2014) 254-263.
- 423 [23]Y. H. Su, K. Oikawa, S. Harjo, T. Shinohara, T. Kai, M. Harada, K. Hiroi, S. Y. Zhang,

- 424 J. D. Parker, H. Sato, Y. Shiota, Y. Kiyonagi and Y. Tomota, *Mater. Sci. Eng. A* **675**
425 (2016) 19-31.
- 426 [24] W. A. Dollase, *J. Appl. Crystallogr.* **19** (1986) 267-272.
- 427 [25] A. C. Larson and R. B. Von Dreele, *General Structure Analysis System (GSAS)*, Los
428 Alamos National Laboratory Report LAUR 86-748, Los Alamos National Laboratory,
429 Los Alamos (2004).
- 430 [26] Y. Shiota, H. Hasemi and Y. Kiyonagi, *Phys. Procedia* **88** (2017) 128-133.